



**HAL**  
open science

## Modelling of change in permeability induced by dilatancy for brittle geomaterials

Saïd Rahal, Alain Sellier, Jérôme Verdier

► **To cite this version:**

Saïd Rahal, Alain Sellier, Jérôme Verdier. Modelling of change in permeability induced by dilatancy for brittle geomaterials. *Construction and Building Materials*, 2016, 125, pp.613-624. 10.1016/j.conbuildmat.2016.08.002 . hal-01849704

**HAL Id: hal-01849704**

**<https://hal.insa-toulouse.fr/hal-01849704>**

Submitted on 5 Nov 2018

**HAL** is a multi-disciplinary open access archive for the deposit and dissemination of scientific research documents, whether they are published or not. The documents may come from teaching and research institutions in France or abroad, or from public or private research centers.

L'archive ouverte pluridisciplinaire **HAL**, est destinée au dépôt et à la diffusion de documents scientifiques de niveau recherche, publiés ou non, émanant des établissements d'enseignement et de recherche français ou étrangers, des laboratoires publics ou privés.

# Modelling of change in permeability induced by dilatancy for brittle geomaterials

S. Rahal <sup>a,b,\*</sup>, A. Sellier <sup>b</sup>, J. Verdier <sup>b</sup>

<sup>a</sup> Institut de Recherche en Génie Civil et Mécanique (GeM), Université de Nantes, École Centrale de Nantes, CNRS: UMR 6183, 58 rue Michel Ange, 44600 Saint-Nazaire, France  
<sup>b</sup> Université de Toulouse, UPS, INSA, LMDC (Laboratoire Matériaux et Durabilité des Constructions), 135, avenue de Rangueil, F-31 077 Toulouse Cedex 04, France

---

The safety and durability of concrete structures are significantly affected by cracking. This structural disorder provides a preferential path for the penetration of fluids and may accelerate the material deterioration. This study investigates the mechanical damage and permeability interactions in geomaterials subjected to compressive stress inducing cracking. The development reported here is implemented within an elasto-plastic damage model able to compute plastic dilatancy. The model assumes an initial isotropic permeability tensor which becomes anisotropic with non-isotropic expansion. The model capabilities are highlighted by simulating uniaxial and triaxial compression tests. The simulation results are compared with experimental data.

## 1. Introduction

Cracking in civil engineering structures significantly affects their durability and ultimately their safety. When cracks reach the reinforcement, the load-bearing capacity is decreased and the material deterioration can accelerate. Regarding the transfer properties, cracking leads to leaks and loss of containment ability induced by the increasing permeability as cracks open.

Several experimental studies have been carried out in order to predict the change of permeability caused by damage. For instance, in the case of a localized crack initiated by a split test, it has been shown that permeability variations can be expressed as a function of crack opening [1–6]. When a laminar flow of water or gas is considered, Poiseuille's law has been found appropriate to predict flow rate through the macroscopic crack [3–6].

On the other hand, diffuse cracking, which is the focus of this paper, is usually generated by uniaxial or deviatoric loading [7–15]. In this situation, it has been shown that the change of permeability can be expressed as a function of a damage parameter,  $D$ , proportional to the variation of Young's modulus [10,12,16]. This parameter quantifies the loss of stiffness induced by cracking. It is a scalar quantity, the value of which can range between 0 (healthy material) and 1 (completely damaged material). For instance, exponential [10,12] and logarithmic [16] empirical functions have been proposed to manage permeability variations with respect to the variable,  $D$ .

The experimental results found in [10,12,13] are plotted in Fig. 1 and compared to the proposed empirical functions with respect to  $D$ . These relationships were assumed to be appropriate only when  $D \in [0 - 0.15]$ . As shown in Fig. 1, the ratio of permeabilities between the damaged and healthy samples ( $k/k^0$ ) remains lower than 9 in the pre-peak phase, and does not change significantly with the type of concrete: plain concrete (OC), high-performance concrete (HPC) or high-performance fibre-reinforced concrete (HPFRC) [10]. Other authors [12,13] have found that the

---

\* Corresponding author at: Institut de Recherche en Génie Civil et Mécanique (GeM), Université de Nantes, École Centrale de Nantes, CNRS: UMR 6183, 58 rue Michel Ange, 44600 Saint-Nazaire, France.

E-mail address: rahal-s@univ-nantes.fr (S. Rahal).

URL: <https://gem.ec-nantes.fr/> (S. Rahal).

## Nomenclature

Name	Symbol		
$\mathbb{C}$	fourth-order stiffness tensor	$\Delta_{jj}$	equivalent crack spacing in the $j$ direction
$\boldsymbol{\varepsilon}^e$	elastic strain tensor	$\Delta$	isotropic equivalent crack spacing used to compute $\mathbf{k}^{\text{eq},s}$
$\boldsymbol{\varepsilon}^{pl,s}$	plastic strain tensor including dilatancy	$k^0$	initial isotropic permeability
$\boldsymbol{\sigma}$	total stress tensor	$k_i^F$	permeability of the $i$ th crack
$\tilde{\boldsymbol{\sigma}}$	undamaged stress tensor	$w_{ij}^i$	crack opening of the $i$ th crack in the $j$ direction
$\tilde{\boldsymbol{\sigma}}^d$	deviatoric part of the undamaged stress tensor $\tilde{\boldsymbol{\sigma}}$	$Q_j^{\text{tot}}$	total flow in the $j$ direction
$\mathbf{k}^{\text{eq},s}$	induced anisotropic permeability tensor due to dilatancy	$Q_j^0$	flow through the healthy part of the material in the $j$ direction
$f^{\text{DP}}$	Drucker–Prager plastic criterion	$Q_j^F$	flow through the cracks in the $j$ direction
$\delta$	Drucker–Prager coefficient	$\ell_{jj}$	size of the finite element in the $j$ direction
$\phi$	friction angle	$n$	number of cracks
$F^{\text{DP}}$	non-associated Drucker–Prager yield function	$E^0$	initial isotropic Young’s modulus
$\beta$	dilatancy coefficient	$\nu^0$	initial isotropic Poisson’s ratio
$d^s$	isotropic shear damage	$R_0^c$	threshold stress to initiate plastic dilatancy
$\varepsilon^{\text{th},s}$	dilatancy threshold used to compute $d^s$	$R^c$	compression peak strength
$\varepsilon^{k,s}$	characteristic strain used to compute $d^s$	$\varepsilon^{\text{peak},c}$	strain at $R^c$
$\varepsilon^{\text{th},p}$	strain percolation threshold used to compute $\mathbf{k}^{\text{eq},s}$	$\sigma^0$	confining pressure

ratio  $(k/k^0)$  remains lower than 4 (for plain concrete). As will be shown in the next section, these differences can be attributed to the directions of flow measurements (according to the induced anisotropy of cracking in a uniaxial compression test). For instance, in reference [10], the measurements were carried out in the same direction as loading, while in references [12,13], the authors made them in the direction perpendicular to the loading.

When  $D \in [0.15 - 1]$ , especially after the peak of the behaviour law, the literature provides a group of empirical relationships which have to be fitted according to experimental results and finite element sizes in order to predict realistic permeability variations [17,20,19]. As shown in Fig. 2, the empirical logarithmic function proposed in [19] gave a reasonable fit for the experimental permeability variations under the uniaxial compression test found in [12]. The relationship proposed in [16], which was fitted on tensile test [18,21] (see [21] for more details on the experimental device) also seemed to give good agreement with measurements too. We recall that, in pre-peak phase, this relation was fitted on a uniaxial compression test [10].

In a first step, the mechanisms observed to be involved during uniaxial compression or deviatoric loading leading to increased permeability are highlighted and the drawbacks of previous simplified damage formulations are pointed out. The second step of this work focuses on the proposed anisotropic permeability model, which is fundamentally based on the damage model [22] enhanced by a coupling with non-standard plasticity (implemented in CAST3M finite element program [23]). The model results are compared to mechanical and permeability measurements. Finally, tri-axial tests are simulated in order to demonstrate the relevance of such modelling.

## 2. Change of permeability under compression loading

### 2.1. Drawback of damage-permeability relationship

As suggested by experimental results [10,12,14] and usually adopted in numerical modelling, the change of permeability can

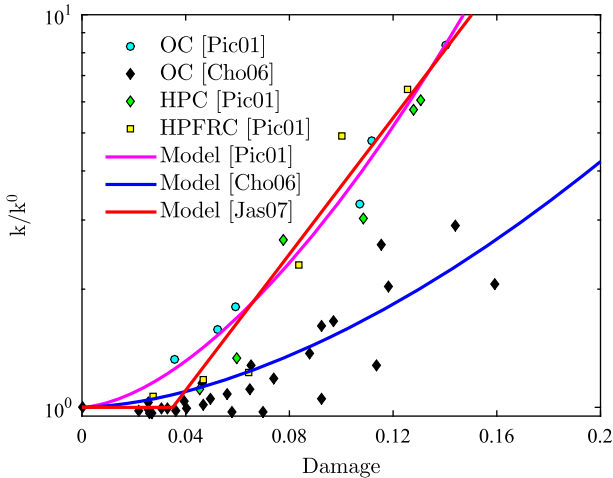


**Fig. 1.** Predicted variations of permeability ratio  $(k/k^0)$  [10,12,16] with respect to the damage parameter: comparison with experimental permeability measurements [10,12].

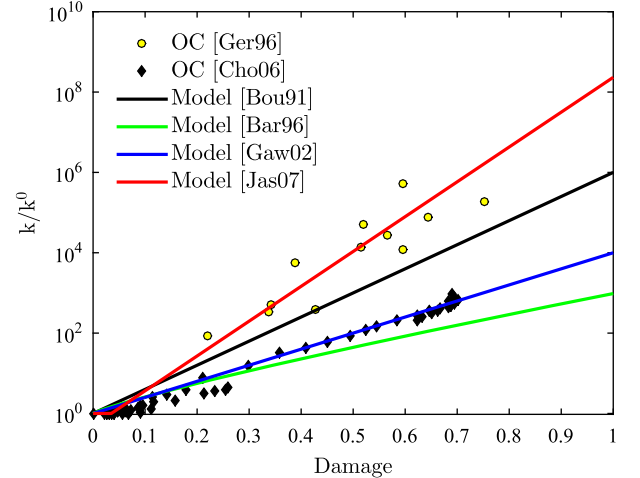


**Fig. 2.** Predicted variations of permeability ratio  $(k/k^0)$  [17–19,16] with respect to the damage parameter: comparison with experimental permeability measurements [18,12].

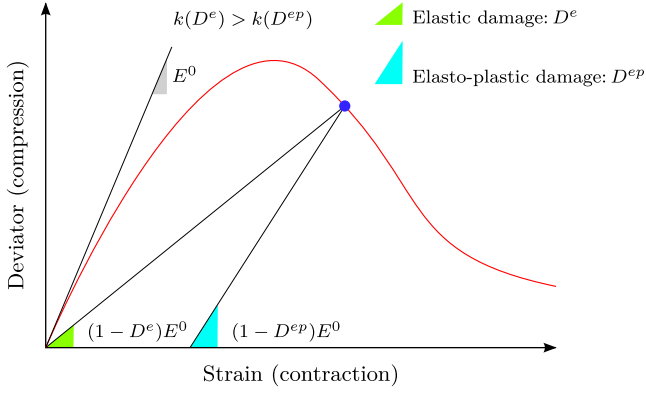


**Fig. 3.** Schematic comparison between elastic and elasto-plastic damage parameter under compressive or deviatoric loading.

be expressed as a function of an isotropic [19,24,12,16,25] or anisotropic [26,18,27,28] damage parameter.

Therefore, the damage state when  $D \rightarrow 1$  is not unique regarding crack opening, which makes these models inappropriate for computing permeability in strongly damaged materials. Moreover, the law will be different according to whether the damage model is elastic or elasto-plastic. Fig. 3 shows the conventional nature of damage and consequently the limit of considering a permeability-damage relationship.

For instance, let us consider the function proposed in [16] to predict permeability. If the damage parameter is overestimated, an error of 0.1 leads to a permeability being misestimated by a factor greater than 7. This error might increase exponentially according to the evolution of permeability.

More particularly, computing the damage parameter according to the slope from the origin of the stress-strain curve (elastic damage formulation) leads to ( $D^e = 0.42$ ) at the peak of the behaviour law in the case of a uniaxial compression test (considering an ordinary concrete with:  $E^0 = 18000$  MPa,  $R^c = 28$  MPa and  $\varepsilon^{\text{peak,c}} = 2.7 \times 10^{-3}$  [12]):

$$D^e = \frac{E^0 - E^D}{E^0} = \frac{E^0 - R^c / \varepsilon^{\text{peak,c}}}{E^0} = 0.42 \quad (1)$$

On the other hand, if permanent strains are assumed (as observed experimentally), the measured damage during unloading was close to 0.15 [10,12]. As a result, the permeability will be overestimated 200 times at the peak of the behaviour law in the elastic

damage formulation. Consequently, resorting to a more objective variable than  $D$ , such as plastic strains or crack openings, could be more realistic.

The next section presents the different phases for permeability evolution evidenced under/after loading according to a review of the literature. These phenomena have to be taken into account when modelling permeability variation under compressive or deviatoric loading.

## 2.2. Experimental observations

Experimental results on concrete [7,12], mortar [8,9], rock salt [11] and granite [14,15] suggest a behaviour under compressive or deviatoric loading that can be divided into 3 parts:

1. When loading begins, the permeability decreases slightly. This phenomenon is usually attributed to the reduction of porosity and/or to the closure of initial microcracks induced by the drying procedure (associated with gas permeability measurements). This phase corresponds to the material elasticity (volumetric strain contractancy).
2. In the second phase, expansion increases slightly and permeability remains relatively constant. This seems to indicate that there is a balance between the consolidation due to the mean stress and the occurrence of new microcracks.
3. In the last phase, dilatancy increases more significantly, and a noticeable increase in permeability is observed. This situation occurs at approximately 70–90% of the peak strength.

These phases are summarized in the scheme presented in Fig. 4.

When phases 1 and 2 are considered, a model including a threshold parameter as proposed in [16,14,28] is realistic. On the other hand, a model including plastic dilatancy might be more appropriate for phase 3. The next section presents the mechanical model that allows permeability variations to be computed anisotropically thanks to plastic dilatancy.

## 2.3. Description of the elasto-plastic damage model

The mechanical model presented below is based on the initial formulation, as described in [22], to which additional plastic strains are added. With these modifications, the model is especially suited to managing the 3 phases as described previously.

1. When loading begins and does not exceed the initial threshold needed to initiate plasticity,  $\bar{R}_0^c$  (which will be defined in 2, below), the mechanical behaviour is purely elastic:

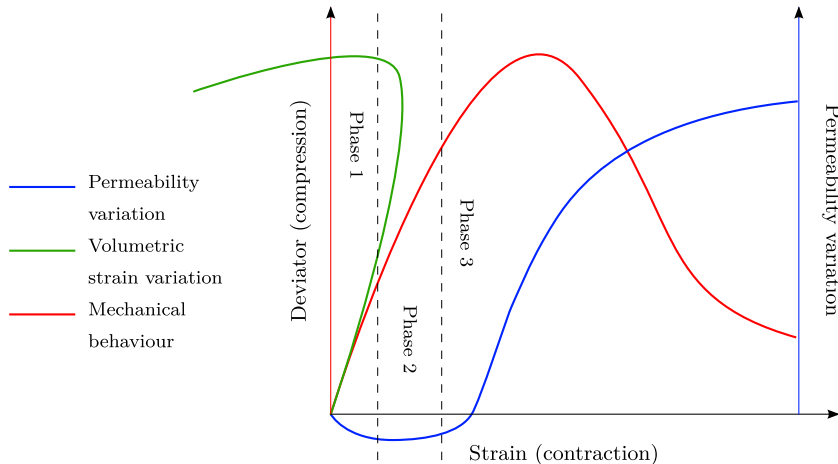


**Fig. 4.** Typical permeability evolution under compressive or deviatoric loading as observed in the literature.

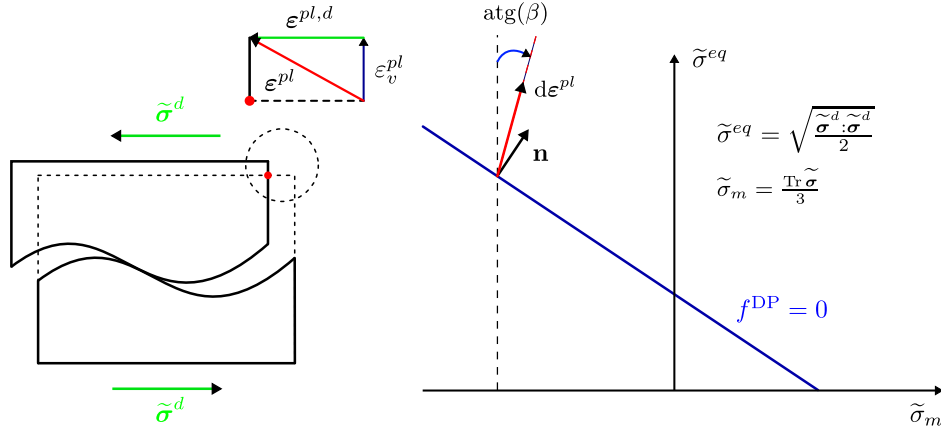


Fig. 5. Schematic representation and physical interpretation of the dilatancy coefficient  $\beta$ .

$$d\tilde{\sigma} = \mathbb{C} : d\boldsymbol{\varepsilon}^e \quad (2)$$

where  $\mathbb{C}$  is the fourth-order stiffness tensor,  $\tilde{\sigma}$  is the undamaged stress tensor and  $\boldsymbol{\varepsilon}^e$  is the elastic strain tensor.

- When the initial threshold,  $\tilde{R}_0^c$ , is exceeded and before the peak of the behaviour law, diffuse micro-cracking is initiated. In this stage, a positive parabolic hardening is used. The parabolic hardening function is adjusted in such a way that the stress-strain curve reaches the peak point of the behaviour law ( $R^c, \boldsymbol{\varepsilon}^{\text{peak},c}$ ) in the case of a uniaxial compression test. In multi-axial conditions, the peak depends on the hydrostatic pressure. This phenomenon is modelled using the Drucker-Prager plastic criterion,  $f^{\text{DP}}$ , defined as follows:

$$f^{\text{DP}} = \sqrt{\frac{\tilde{\sigma}^d : \tilde{\sigma}^d}{2} + \frac{\delta}{3} \text{Tr} \tilde{\sigma}} - \tilde{R}^c \left( \frac{\sqrt{3}}{3} - \frac{\delta}{3} \right) \quad (3)$$

where  $\tilde{\sigma}^d$  is the deviatoric part of the undamaged stress tensor  $\tilde{\sigma}$ ,  $\text{Tr} \tilde{\sigma}$  represents its trace and  $\delta$  corresponds to the Drucker-Prager coefficient. As shown in Eq. (3), in the case of a uniaxial compression test in the  $z$  direction, it leads to ( $f^{\text{DP}} = \tilde{\sigma}_{zz} - \tilde{R}^c$ ). In this phase, a non-associated Drucker-Prager yield function,  $F^{\text{DP}}$ , is used to compute dilatancy:

$$F^{\text{DP}} = \sqrt{\frac{\tilde{\sigma}^d : \tilde{\sigma}^d}{2} + \frac{\beta}{3} \text{Tr} \tilde{\sigma}} \quad (4)$$

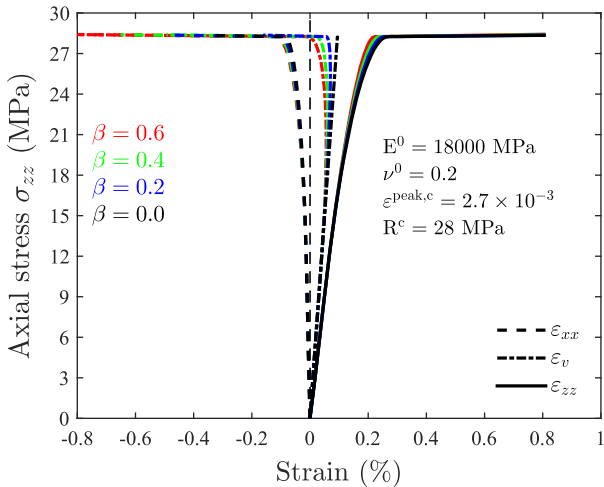


Fig. 6. Evolutions of the axial stress,  $\sigma_{zz}$ , with respect to the axial,  $\varepsilon_{zz}$ , radial,  $\varepsilon_{xx}$ , and volumetric strains,  $\varepsilon_v$ , in uniaxial compression test.  $\beta \in \{0, 0.2, 0.4, 0.6\}$ .

where  $\beta$  is the dilatancy coefficient. It was introduced to manage the increase of volumetric strain in function of the deviatoric strain. The dilatation is the consequence of the change of inelastic volume due to plastic deviation. Fig. 5 represents the dilatancy coefficient in the equivalent Drucker-Prager stress/mean stress plane as defined in Eq. (4).

The Lagrange multiplier increments,  $d\lambda$ , are computed with respect to classical Kuhn-Tucker conditions and allow the plastic strain tensor increment,  $d\boldsymbol{\varepsilon}^{pl,s}$ , to be deduced:

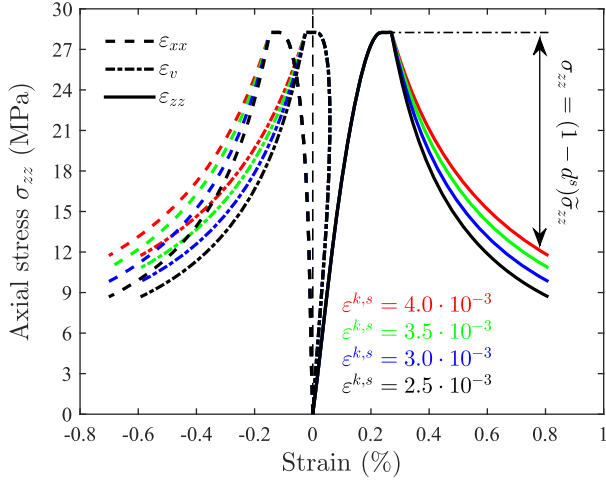
$$d\boldsymbol{\varepsilon}^{pl,s} = d\lambda \frac{\partial F^{\text{DP}}}{\partial \tilde{\sigma}} \quad (5)$$

Fig. 6 presents the evolutions of the axial stress,  $\sigma_{zz}$ , with respect to the axial,  $\varepsilon_{zz}$ , radial,  $\varepsilon_{xx}$ , and volumetric,  $\varepsilon_v$ , strains for the case of a uniaxial compression test in the  $z$  direction (compression and contraction are assumed positive here for readability). The fixed material properties considered for the parametric study are written in Fig. 6 and they corresponded to those found for an ordinary concrete in [12]. The uniaxial test was performed 4 times, changing the value of dilatancy coefficient ( $\beta \in \{0, 0.2, 0.4, 0.6\}$ ). As shown by this Figure, the increasing dilatancy coefficient affects the radial strain behaviour (and consequently the volumetric strain variation) only by increasing expansion.

- Plasticity was used to limit the undamaged stress tensor,  $\tilde{\sigma}$  (see Fig. 6). If some residual material remains undamaged during the damage process, this means that its effective strength is greater than that of the material already damaged. The computed damage associated with the Drucker-Prager criterion is assumed to be increased by volumetric dilatancy, ( $\text{Tr} \boldsymbol{\varepsilon}^{pl,s}$ ). The model assumes that dilatancy leads to isotropic damage, noted  $d^s$ , only if it is greater than a dilatancy threshold,  $\varepsilon^{th,s}$ , which corresponds to the trace of the plastic strain tensor at the peak of the behaviour law, ( $\text{Tr} \boldsymbol{\varepsilon}_{\text{peak}}^{pl,s}$ ), in the case of a uniaxial compression test. The shear damage density,  $d^s$ , is defined as follows:

$$d^s = \begin{cases} 0 & \text{if } \text{Tr} \boldsymbol{\varepsilon}^{pl,s} \leq \varepsilon^{th,s} \\ \frac{\text{Tr} \boldsymbol{\varepsilon}^{pl,s} - \varepsilon^{th,s}}{\text{Tr} \boldsymbol{\varepsilon}^{pl,s} - \varepsilon^{th,s} + \varepsilon^{k,s}} & \text{if } \text{Tr} \boldsymbol{\varepsilon}^{pl,s} > \varepsilon^{th,s} \end{cases} \quad (6)$$

where  $\varepsilon^{k,s}$  is the characteristic strain used to control the damage evolution versus dilatancy. Obviously the damage  $d^s$  could be computed before the peak of the behaviour law too (since dilatancy is also available in this phase). However, this was not considered in the present modelling because pre-peak non linearity was modelled in a simplified way using plasticity. On the other hand, the induced loss of stiffness has been



**Fig. 7.** Evolutions of the axial stress,  $\sigma_{zz}$ , with respect to the axial,  $\varepsilon_{zz}$ , radial,  $\varepsilon_{xx}$ , and volumetric strains,  $\varepsilon_v$ , in uniaxial compression test.  $\varepsilon^{k,s} \in \{2.5, 3.0, 3.5, 4.0\} \times 10^{-3}$ .

found almost negligible before the peak of the behaviour law in uniaxial compression tests ( $d^s < 0.15$  according to [10,12]). Fig. 7 presents the evolutions of the axial stress,  $\sigma_{zz}$ , with respect to the axial,  $\varepsilon_{zz}$ , radial,  $\varepsilon_{xx}$ , and volumetric,  $\varepsilon_v$ , strains, for a uniaxial compression test in the  $z$  direction. The uniaxial test was performed 4 times (assuming  $\beta = 0.45$ ), changing the value of the characteristic strain ( $\varepsilon^{k,s} \in \{2.5, 3.0, 3.5, 4.0\} \times 10^{-3}$ ). As shown by Eq. (6), when  $\varepsilon^{k,s}$  decreases,  $d^s$  increases and consequently leads to increasingly brittle behaviour, as shown in Fig. 7.

The elasto-plastic damage model described above is able to compute plastic dilatancy. As explained in Section 2.2, permeability increases when dilatancy is initiated. Consequently, permeabilities should be computed with respect to the plastic strain dilatancy provided by the model. The next section explains how dilatancy is used to assess anisotropic permeabilities.

#### 2.4. Permeability modelling

Fig. 8 represents a finite element including diffuse cracking perpendicular to the  $z$  direction. The idealized cracking scheme in Fig. 8 could be due to compression in the  $x$  direction. In fact, compression in the  $x$  direction also leads to diffuse cracking perpendicular to the  $y$  direction. However, in a first step, we focus on cracking perpendicular to the  $z$  direction.

In order to compute the flow rate in the  $x$  direction, the contributions of the following must be considered:

- each fracture, with permeability  $k_i^F$ ,
- the residual healthy material between cracks, with permeability  $k^0$ .

Regarding the fracture permeabilities, for the case of one localized crack initiated by a split test, it has been shown that permeability can be computed according to Poiseuille's law (considering laminar flow) [3–6]. In this work, each fracture permeability evolution,  $K_i^F$ , is assumed to be driven by Poiseuille's law and is computed using the following formula:

$$k_i^F = \frac{(w_{zz}^i)^2}{12} \quad (7)$$

where  $w_{zz}^i$  represents the crack opening of each fracture. Using the equivalence principle, it is possible to consider only a homogeneous equivalent material with permeability,  $k_{xx}^{eq,s}$ , in the  $x$  direction (see Fig. 8).

The total flow in the  $x$  direction,  $Q_x^{tot}$ , corresponds to the sum of flow through the cracks,  $Q_x^F$ , and flow through the healthy part,  $Q_x^0$ :

$$Q_x^{tot} = Q_x^0 + Q_x^F \quad (8)$$

The equivalent permeability,  $k_{xx}^{eq,s}$ , can be deduced by writing Darcy's law and considering the flow rate in the  $x$  direction:

$$k_{xx}^{eq,s}(\ell_{yy}\ell_{zz}) = \overbrace{k^0 \ell_{yy} \left( \ell_{zz} - \sum_{i=1}^n w_{zz}^i \right)}^{\text{healthy part}} + \overbrace{\sum_{i=1}^n \frac{\ell_{yy}}{12} (w_{zz}^i)^3}^{\text{cracks contribution}} \quad (9)$$

Without information on the distribution of the cracks and their apertures, all crack openings are assumed to be equal to  $w_{zz}$  and a homogeneous cracking distribution is assumed ( $n$  is the number of cracks). The mean crack spacing is ( $\Delta_{zz} = \ell_{zz}/n$ ) and leads to:

$$k_{xx}^{eq,s} = k^0 \left( \frac{\ell_{zz} - n \cdot w_{zz}}{\ell_{zz}} \right) + \frac{n}{\ell_{zz}} \cdot \frac{(w_{zz})^3}{12} \quad (10)$$

Assuming that crack widths are smaller than the finite element size ( $nw_{zz} \ll \ell_{zz}$ ), the equivalent permeability,  $k_{xx}^{eq,s}$ , can be deduced:

$$k_{xx}^{eq,s} = k^0 + \frac{(w_{zz})^3}{12\Delta_{zz}} \quad (11)$$

The following approximation involving plastic dilatancy in the  $z$  direction,  $\varepsilon_{zz}^{pl,s}$ , is used to compute crack opening:

$$w_{zz} = \Delta_{zz} \langle \varepsilon_{zz}^{pl,s} - \varepsilon^{th,p} \rangle_+ \quad (12)$$

here  $\langle \cdot \rangle_+$  is the function of the positive part. It is defined such that  $\langle \kappa \rangle_+ = \max(0, \kappa)$  and was introduced to consider the strain percolation threshold,  $\varepsilon^{th,p}$ , used to compute permeability as observed in phases 1 and 2 described in Section 2.2.

Finally, the equivalent permeability,  $k_{xx}^{eq,s}$ , is deduced using the following formula:

$$k_{xx}^{eq,s} = k^0 + \Delta_{zz}^2 \frac{\langle \varepsilon_{zz}^{pl,s} - \varepsilon^{th,p} \rangle_+^3}{12} \quad (13)$$

Eq. (13) is valid in the  $x$  direction. However this approximation is also appropriate in the  $y$  direction and leads to:

$$k_{yy}^{eq,s} = k^0 + \Delta_{zz}^2 \frac{\langle \varepsilon_{zz}^{pl,s} - \varepsilon^{th,p} \rangle_+^3}{12} \quad (14)$$

In the  $z$  direction, we must consider the equality of flow rates, which does not modify the flow perpendicular to the cracks. As mentioned previously, compression in the  $x$  direction would lead to cracking perpendicular to the  $y$  direction too. These cracks are assumed to be separated by an equivalent spacing,  $\Delta_{yy}$ . However, in initially isotropic materials, the aggregates are usually randomly distributed and it is possible to consider an isotropic equivalent crack spacing,  $\Delta$  ( $\Delta_{yy} = \Delta_{zz} = \Delta$ ). In this situation, permeability in the  $z$  direction,  $k_{zz}^{eq,s}$ , is increased and computed according to the following formula:

$$k_{zz}^{eq,s} = k^0 + \Delta^2 \frac{\langle \varepsilon_{yy}^{pl,s} - \varepsilon^{th,p} \rangle_+^3}{12} \quad (15)$$

As a result, the permeability in the  $x$  direction becomes:

$$k_{xx}^{eq,s} = k^0 + \Delta^2 \frac{\langle \varepsilon_{zz}^{pl,s} - \varepsilon^{th,p} \rangle_+^3}{12} + \Delta^2 \frac{\langle \varepsilon_{yy}^{pl,s} - \varepsilon^{th,p} \rangle_+^3}{12} \quad (16)$$

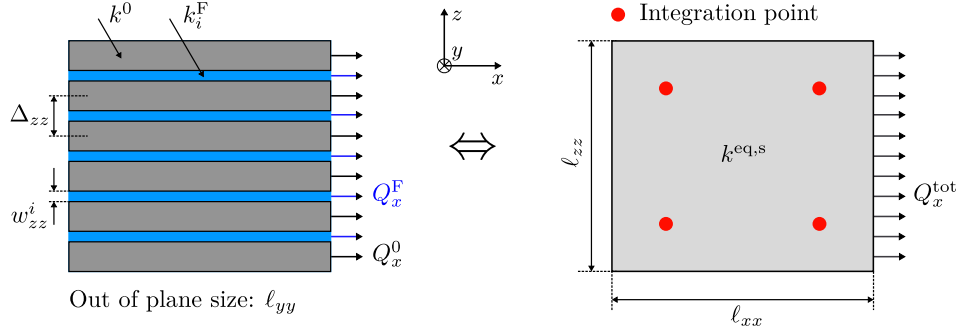


**Fig. 8.** Idealized finite element subjected to parallel diffuse cracking.  $w_{zz}^i$  is the crack aperture of each crack in the  $z$  direction,  $\Delta_{zz}$  is the equivalent crack spacing,  $\ell_{xx}$ ,  $\ell_{yy}$  and  $\ell_{zz}$  are the finite element sizes in the corresponding directions.

Finally, the following general form is used to compute anisotropic permeabilities related to shear damage:

$$\begin{cases} k_{xx}^{eq,s} = k^0 + \Delta^2 \left( \frac{(\epsilon_{yy}^{pl,s} - \epsilon^{th,p})_+^3}{12} + \frac{(\epsilon_{zz}^{pl,s} - \epsilon^{th,p})_+^3}{12} \right) \\ k_{yy}^{eq,s} = k^0 + \Delta^2 \left( \frac{(\epsilon_{xx}^{pl,s} - \epsilon^{th,p})_+^3}{12} + \frac{(\epsilon_{zz}^{pl,s} - \epsilon^{th,p})_+^3}{12} \right) \\ k_{zz}^{eq,s} = k^0 + \Delta^2 \left( \frac{(\epsilon_{xx}^{pl,s} - \epsilon^{th,p})_+^3}{12} + \frac{(\epsilon_{yy}^{pl,s} - \epsilon^{th,p})_+^3}{12} \right) \end{cases} \quad (17)$$

The equations defined in system (17) are written in the principal directions of the plastic strain tensor including dilatancy,  $\epsilon^{pl,s}$ . Consequently, the directions  $x$ ,  $y$  and  $z$  represent the main directions of irreversible strains (eigenvalues). Once the permeability components are computed in the principal directions of the plastic strain tensor, the permeability tensor is then changed in the global basis. As the permeabilities are computed at the Gauss points, in the case of non-uniform plastic strains in the element, the permeability components also become a non-uniform field in accordance with the non-uniform plastic strains.

The next section tests the model, with uniaxial and triaxial tests. The model results are compared to experimental permeability measurements found in the literature.

### 3. Model validation and capability

#### 3.1. Change of permeability under uniaxial compression test

In order to demonstrate the relevance of the permeability model (17), a uniaxial compression test was used to predict axial and radial permeabilities. The uniaxial compression test corresponded to the one presented in [12] on ordinary concrete (hollow cylindrical specimen with external/internal diameters of 110/14 mm and height of 220 mm).

The mechanical parameters used for this study are given in Table 1. Three parameters ( $\epsilon^{k,s}$ ,  $\beta$  and  $\delta$ ) were fitted according to experimental mechanical results (the others were provided by [12]). The influence of each parameter, especially  $\beta$  and  $\epsilon^{k,s}$  was highlighted previously in Figs. 6 and 7.

As shown in Table 1, the concrete Young's modulus seems rather low. This could be explained by the use of an important water/cement ratio in [12,13] ( $w/c = 0.6$ ), leading to reduce mechanical performances. In addition, the value of 18000 MPa corresponded to the one measured on a specimen after drying at 105 °C, while the initial Young's modulus was 23000 MPa 1 month after wet cure [13]. The effect of drying on mechanical behaviour was evidenced in [29]. It led to a decreasing stiffness due to the development of microcracks.

**Table 1**

Mechanical parameters for the uniaxial compression test simulation. \* corresponds to the parameters estimated to fit the experimental results.

Mechanical parameter	Symbol	Value	Unit
Initial Young's modulus	$E^0$	18000	MPa
Initial Poisson's ratio	$\nu^0$	0.2	
Threshold stress to initiate dilatancy*	$R_0^c$	14	MPa
Compression peak strength	$R^c$	28	MPa
Strain at $R^c$	$\epsilon^{peak,c}$	$2.7 \times 10^{-3}$	
Characteristic strain*	$\epsilon^{k,s}$	$3.5 \times 10^{-3}$	
Dilatancy coefficient*	$\beta$	0.45	
Drucker-Prager coefficient*	$\delta$	0.72	

In this modelling, a friction angle ( $\phi = 31$  deg) is assumed for normal strength concrete as found in [30], which allows the Drucker-Prager coefficient,  $\delta$ , to be computed:

$$\delta = \frac{2\sqrt{3} \sin(\phi)}{3 - \sin(\phi)} = 0.72 \quad (18)$$

However, in a uniaxial compression test as simulated here, the coefficient,  $\delta$ , has no incidence on the mechanical behaviour; only the dilatancy coefficient,  $\beta$ , is of importance.

Fig. 9 presents the evolutions of the computed axial stress with respect to the computed axial, radial and volumetric strains for a uniaxial compression test. Fig. 9 indicates good agreement with experimental strain measurements thanks to the fact that the

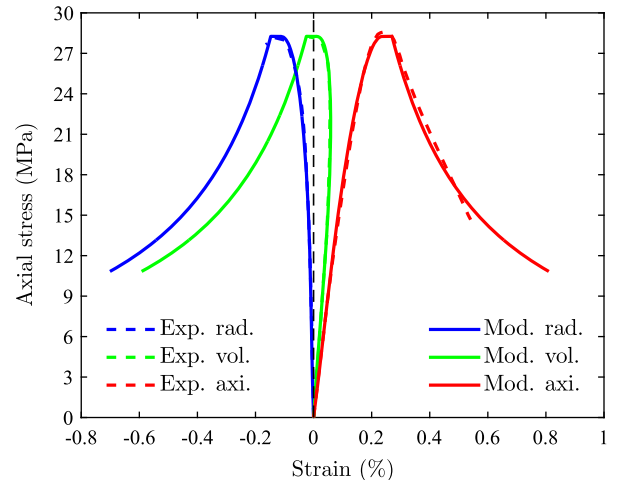


**Fig. 9.** Evolutions of the axial stress with respect to the axial, radial and volumetric strains: comparison with experimental measurements (dashed points) found in [12].

plastic-damage model allows both damage ( $\varepsilon^{k,s} = 3.5 \times 10^{-3}$ ) and dilatancy ( $\beta = 0.45$ ) to be fitted.

As explained in [12], gas permeability measurements were conducted while the specimen was loaded and unloaded. In these tests, the flow measurements were made radially. The change of radial permeability ratio (damaged material permeability/initial material permeability) in function of the uniaxial strain ratio ( $\varepsilon^{\text{axial}}/\varepsilon^{\text{peak,c}}$ ) is plotted in Fig. 10 as found in [12] (the initial intrinsic permeability was ( $k^0 = 9.10^{-17} \text{ m}^2$ ) [12]). In this simulation, the value of the threshold parameter,  $\varepsilon^{\text{th,p}}$ , was chosen to make the increasing value of strain ratio compatible with permeability measurements, thus leading to ( $\varepsilon^{\text{th,p}} = 0.13\varepsilon^{\text{peak,c}}$ ). In order to compute the equivalent crack spacing from experimental results, the permeability measurements were expressed with respect to plastic dilatancy. Fig. 11 represents the evolution of plastic dilatancy with respect to the uniaxial strain ratio. In this figure, the experimental data were projected on numerical results (to extract the contribution of dilatancy) and allowed the computation of the equivalent

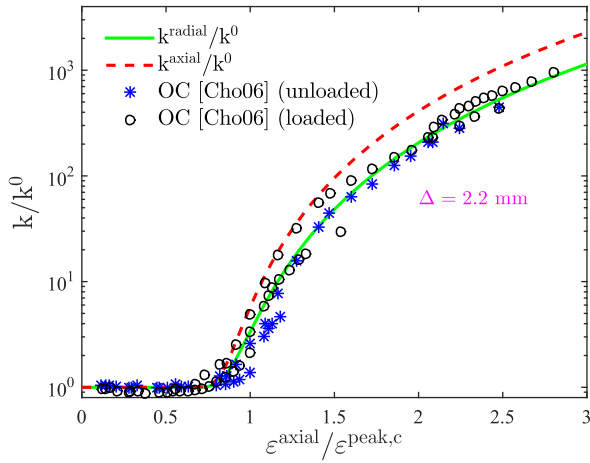


**Fig. 10.** Evolutions of the computed intrinsic axial and radial permeability ratios under uniaxial compression with respect to the uniaxial strain ratio: comparison with experimental radial permeability measurements [12].

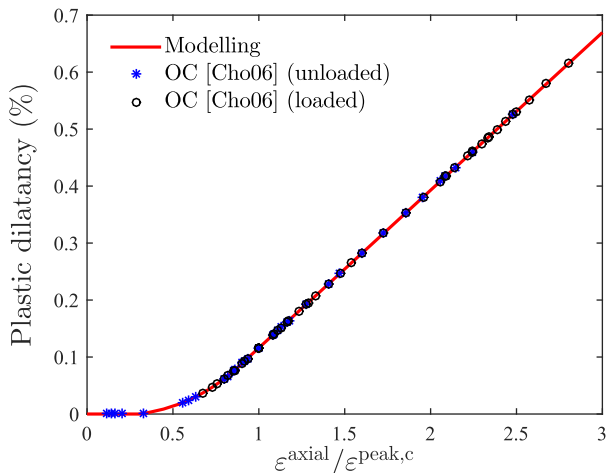


**Fig. 11.** Evolution of plastic dilatancy with respect to the uniaxial strain ratio for concrete: projection of experimental data on numerical results.

crack spacing,  $\Delta_i$ , for each experimental point using the following formula in Eq. (19) obtained by inversion of Eq. (17):

$$\Delta_i = \sqrt{12 \frac{k_i^{\text{radial}} - k^0}{(\varepsilon_i^{\text{pl,s}} - \varepsilon^{\text{th,p}})^3}} \quad \text{with} \quad \begin{cases} k_i^{\text{radial}} - k^0 \geq 0 \\ \varepsilon_i^{\text{pl,s}} - \varepsilon^{\text{th,p}} > 0 \end{cases} \quad (19)$$

Fig. 12 represents the evolution of the computed equivalent crack spacings,  $\Delta_i$ , with respect to plastic dilatancy. The values of  $\Delta_i$  ranges between [0.9–3.2] mm when the value of plastic dilatancy is lower than 0.3%. When plastic dilatancy is greater than 0.3%,  $\Delta_i$  remains between the interval of [2.0–2.4] mm. As  $\Delta_i$  was randomly distributed around the average value of 2.2 mm (see Fig. 12), this value was assumed in the simulation and it allowed (as shown in Fig. 10) to obtain a good agreement with the experimental radial permeability measurements [12]. The parameter  $\Delta$  could be considered as a material property, certainly depending on the proportion and the shape/size of the concrete aggregates.

Obviously, experimental cracks were not uniformly spaced and the crack openings varied as did the cracking tortuosity, which was not considered here. The random nature of cracking could be taken into account for permeability using homogenization theory (see [31,27,32] for examples).

In fact, the effects of roughness and tortuosity of cracks could be roughly accounted for by introducing a reduction factor,  $\xi$ , when computing the crack permeability in Eq. (7), as is usually done for tensile cracking that has been initiated by a split test [3–6]:

$$k^F = \xi \frac{w^2}{12} \quad (20)$$

For instance, in the case of ordinary concrete (OC),  $\xi$ , was found to be 0.03 [4]. This assumption would lead the crack spacing to increase to ( $\Delta = 12.7 \text{ mm}$ ), which might be more realistic because it is closer to the aggregate sizes used in [12] [4–12.5] mm. With this assumption on  $\xi$ , the crack spacing could be controlled by the aggregate size, which is physically acceptable in the sense that cracks propagate avoiding aggregates. However, it is quite impossible to accurately separate the contributions of crack spacing and tortuosity. Furthermore, it would have no incidence on the shape of permeability curves. For these reasons, the model was not modified, and the idealized parallel crack spacing was kept.

Despite these approximations, Fig. 13, which illustrates the effect of dilatancy on the axial permeability ratio, ( $k^{\text{axial}}/k^0$ ), indicates reasonable agreement with the experimental axial

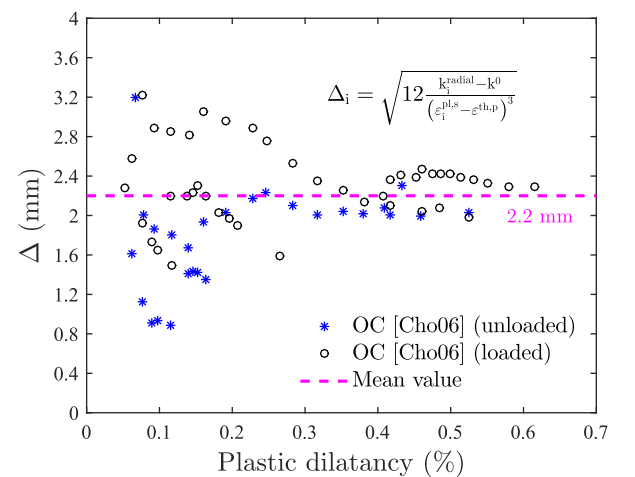


**Fig. 12.** Evolution of the equivalent crack spacing for concrete with respect to plastic dilatancy.

permeability measurements found in [10] (cylinders of 110 mm diameter and 50 mm height), which were conducted on ordinary concrete (OC), high-performance concrete (HPC) and high-performance fibre reinforced concrete (HPFRC). The results presented were obtained with the same set of parameters, without any additional fitting. However, the predicted axial permeability ratio seems to be slightly underestimated with regard to measurements. In fact, the experimental points plotted in Fig. 13 have to be taken cautiously as far as the predicted permeability ratio, ( $k^{\text{axial}}/k^0$ ), is concerned because the initial permeability used in the uniaxial test simulation was ( $k^0 = 9.10^{-17} \text{ m}^2$ ) as found in [12], while it was slightly different in [10] ( $k^0 = 5.10^{-17} \text{ m}^2$ ), ( $k^0 = 2.10^{-17} \text{ m}^2$ ) and ( $k^0 = 2.10^{-17} \text{ m}^2$ ), for OC, HPC and HPFRC, respectively.

In order to compare the simulation results and measurements objectively, the predicted absolute axial permeability variation, ( $k^{\text{axial}} - k^0$ ), is plotted in Fig. 14 and compared to the absolute experimental permeability variation as found in [10]. In this case, a better correspondence with measured values is obtained, especially for ordinary concrete (OC). The variation ( $k^{\text{axial}} - k^0$ ) represents the contribution of cracking only (independently of  $k^0$ ) to axial permeability.

The mean value of 2.2 mm for  $\Delta$  was computed using the permeability measurements obtained on an ordinary concrete with a Young's modulus of 18000 MPa and a compressive peak strength of 28 MPa ( $w/c = 0.6$ ) [12,13]. With the value of 2.2 mm, it was also possible to predict the permeability variations measured on another ordinary concrete with a Young's modulus of 42000 MPa and a compressive peak strength of 65 MPa ( $w/c = 0.49$ ) [10]. The average distribution of aggregates seems to be the main factor that affects crack spacing in concrete. Perhaps some homogenization method considering the aggregate sizes could explain this phenomenon.

In this study,  $\Delta$  was not recalibrated for all types of concrete, because it would require the recalibration of the mechanical parameters too, and the necessary informations were not provided in [10]. However, we can see in Fig. 14 that permeability variations were smaller in the case of a high-performance fibre reinforced concrete (HPFRC). This could be explained by the effect of fibres that diffuse the cracking, thus, leading to a greatest number of

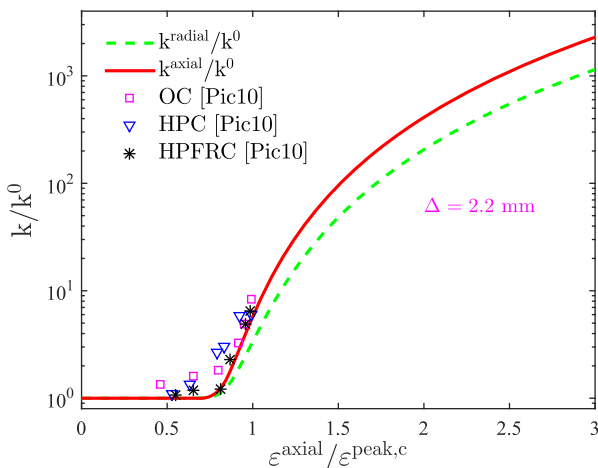


**Fig. 13.** Evolutions of the computed intrinsic axial and radial permeability ratios under uniaxial compression with respect to the uniaxial strain ratio: comparison with experimental axial permeability measurements [10].

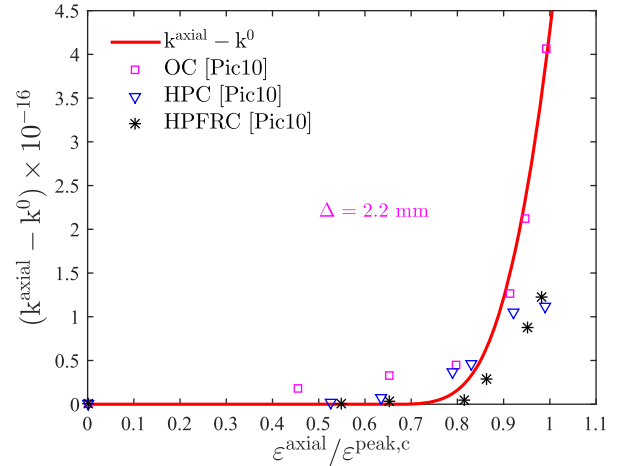


**Fig. 14.** Evolution of the absolute permeability variation ( $k^{\text{axial}} - k^0$ ) with respect to the uniaxial strain ratio: comparison with experimental axial permeability measurements [10].

smaller cracks and, as a consequence, a reduction of the permeability.

Finally, the proposed application gives an understanding of how anisotropy is initiated for permeability in a uniaxial compression test.

Dilatancy was able to explain the anisotropy for permeability components in a uniaxial compression test. The model could be used to predict permeability and its anisotropy for other types of loading able to create expansion. The next section tests the model for the case of triaxial loading.

### 3.2. Change of permeability under triaxial loading

This section investigates the damage and permeability interactions in the case of triaxial tests. The simulation results highlight the main mechanisms taken into account by mechanical and permeability models. The tests were carried out on two different geomaterials, the first triaxial test simulation was performed on mortar and corresponded to the one carried out in [9], the second was performed on granite and corresponded to the one carried out in [32].

#### 3.2.1. Mortar triaxial test simulation

As explained previously, a non-associated Ducker-Prager criterion is used to manage dilatancy and allows the effect of confinement to be considered. Since permeability increases with respect to damage and crack openings, if the peak strength increases with confinement, the permeability should be affected by confinement too. This phenomenon has been observed for granite [14,32] subjected to triaxial loading, it leads to decreasing permeability (at the same axial deformation state or deviatoric stress) when confinement increases.

In the following, a triaxial test is simulated. It takes an initial hydrostatic pressure and then increases axial stress while radial stresses remain constant and equal to the imposed hydrostatic pressure (see Fig. 15).

In this section, the triaxial test performed on mortar is described. As explained in [9], axial gas permeability measurements were performed on mortar specimens under triaxial load. The mortar mechanical parameters (which are not provided in [9]) are noted in Table 2. The Young's modulus,  $E^0$ , and Poisson's ratio,  $\nu^0$ , were deduced from the slope of deviatoric stress/axial strain curves (in the elastic phase).

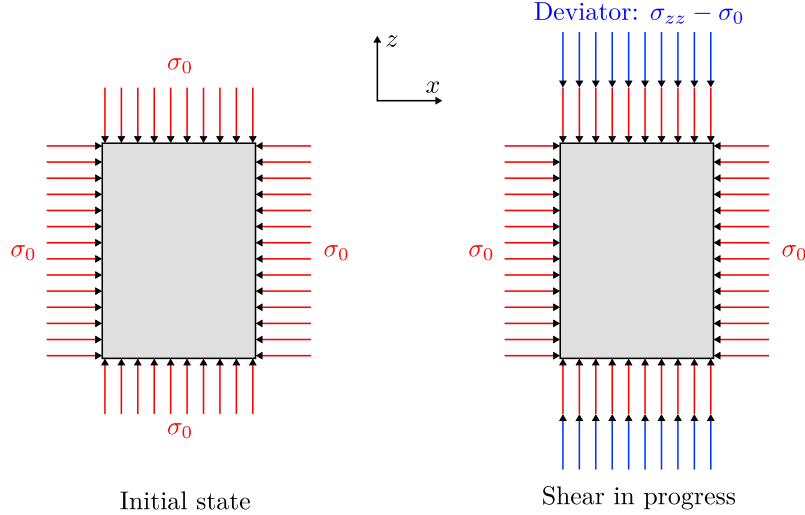


Fig. 15. Principle of triaxial test.

**Table 2**  
Mechanical parameters for simulation of triaxial test on mortar.

Mechanical parameter	Symbol	Value	Unit
Initial Young's modulus	$E^0$	32000	MPa
Initial Poisson's ratio	$\nu^0$	0.15	
Compression peak strength	$R^c$	84.4	MPa
Strain at $R^c$	$\varepsilon^{\text{peak},c}$	$5.5 \times 10^{-3}$	
Characteristic strain	$\varepsilon^{k,s}$	$3.5 \times 10^{-3}$	
Dilatancy coefficient	$\beta$	0.45	
Drucker–Prager coefficient	$\delta$	1.16	

When the confining pressure was 5 MPa, the experimental deviatoric peak strength was 114.5 MPa, but, when the confining pressure was 10 MPa, the experimental deviatoric peak strength was 144.6 MPa [9]. According to the Drucker–Prager criterion, this leads to  $R^c = 84.4$  MPa and allows the friction angle to be deduced:  $\phi = 48.65$  deg, giving  $\delta = 1.16$ . Here,  $R^c$  might seem excessively high, especially for mortar. This could be the consequence of:

1. the small size of the samples (cylinders of 37 mm diameter and 70 mm height), since the probability of defects decreases when specimen size decreases, and consequently peak strength increases [33],
2. the compression peak strength,  $R^c$ , which was computed according to the peak strengths obtained under two different confining pressures (5 and 10 MPa), as found in [9]. This is not enough to predict accurately  $R^c$ , therefore, a third confining pressure would probably provide more informations,
3. the friction between the mechanical device and the mortar sample, which was not considered in the modelling. This phenomenon may increase the apparent strength.

However even the Young's modulus was found to be high for a mortar (see Table 2). This suggests the third assumption to be more relevant.

Here  $\varepsilon^{\text{peak},c}$  was chosen to fit the axial experimental results (positive parabolic hardening behaviour) and  $\beta$  was chosen to make dilatancy compatible with the radial measurements (expansion); it led to the same as found before for concrete ( $\beta = 0.45$ ). Since  $\beta$  was found to be equal for both concrete and mortar, the value of  $\varepsilon^{k,s}$ , which controls the evolution of damage with respect to dilatancy was kept unchanged.

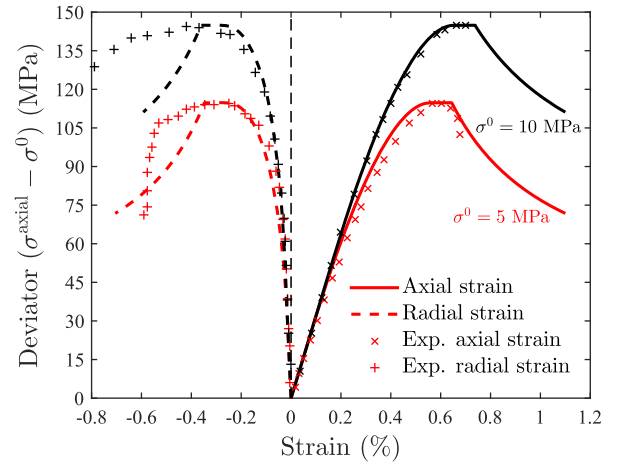


Fig. 16. Evolutions of mortar deviatoric stress with respect to axial and radial strains for different confining pressures (5 and 10 MPa). Comparison with measurements [9].

**Table 3**  
Hydraulic parameters for simulation of mortar triaxial test.

Hydraulic parameter	Symbol	Value	Unit
Intrinsic permeability ( $\sigma^0 = 5$ MPa)	$k^0$	$2.6 \times 10^{-17}$	$\text{m}^2$
Intrinsic permeability ( $\sigma^0 = 10$ MPa)	$k^0$	$1.5 \times 10^{-16}$	$\text{m}^2$
Strain percolation threshold	$\varepsilon^{\text{th},p}$	$0.13\varepsilon^{\text{peak},c}$	
Equivalent crack spacing	$\Delta$	0.14	mm

Fig. 16 presents the evolutions of deviatoric stress with respect to axial and radial strains, obtained under different confining pressures,  $\sigma^0$  (5 and 10 MPa). This figure highlights the same phenomena as those usually observed for concrete under the same loading condition [30]. The mechanical model thus showed reasonable agreement with experimental data [9].

Table 3 introduces the hydraulic parameters considered for this study. This table indicates that the initial intrinsic permeabilities were not the same for the two specimens tested as mentioned in [9]. For this reason, the predicted axial permeabilities are compared to measurements in terms of absolute variation ( $k^{\text{axial}} - k^0$ ) in Fig. 17.

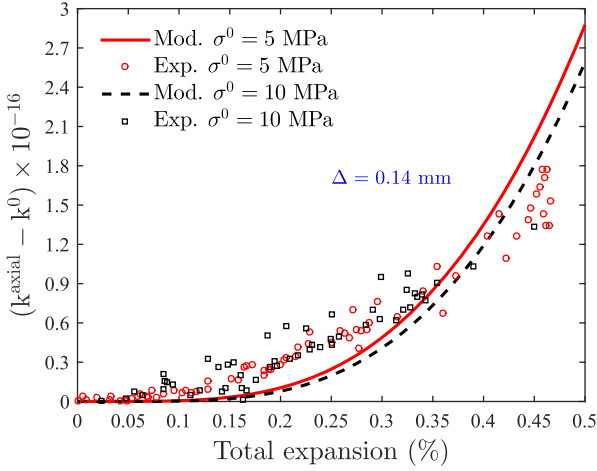


**Fig. 17.** Evolutions of mortar absolute axial permeability ( $k^{\text{axial}} - k^0$ ) with respect to radial strain (expansion) for different confining pressures (5 and 10 MPa). Comparison with measurements [9].

Fig. 17 presents the experimental evolutions of the absolute permeability variations as found in [9], with respect to radial strain (expansion). These variations represent the contribution of cracking to axial permeability. As shown in Fig. 17, there was a very close accordance between both experimental results regardless of the confining pressure (5 and 10 MPa). Initial permeabilities were quite different (see Table 3), thus, permeability variations have to be modelled independently of  $k^0$  as proposed in system (17) and contrary to what has been done previously [10,19,12,16,14,28]. Therefore, if the change of dilatancy with regard to the confining pressure was correctly considered by the mechanical model, then a permeability model based on plastic dilatancy can be used to predict the permeability variations whatever the loading condition and, thus, it justifies the equations proposed in system (17).

In the same way as described for concrete, the equivalent crack spacing was computed for each experimental point. To do so, the experimental permeability measurements initially expressed with respect to the total expansion were projected on plastic dilatancy predicted by modelling in Fig. 18 and allowed the computation of the equivalent crack spacing for each experimental point.

Fig. 19 represents the evolution of the computed equivalent crack spacings with respect to plastic dilatancy. In this figure,  $\Delta$

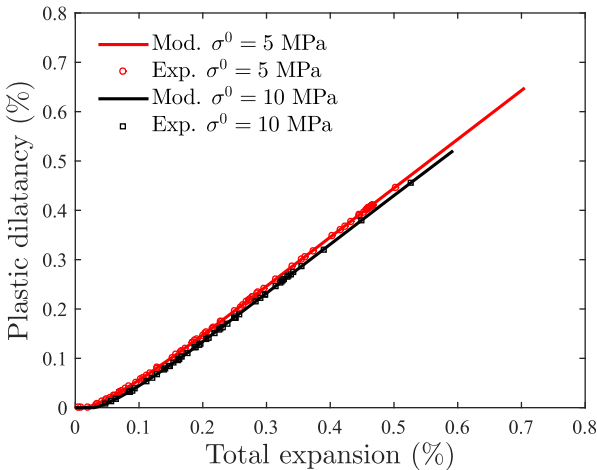


**Fig. 18.** Evolution of plastic dilatancy with respect to the total expansion for mortar: projection of experimental data on numerical results.

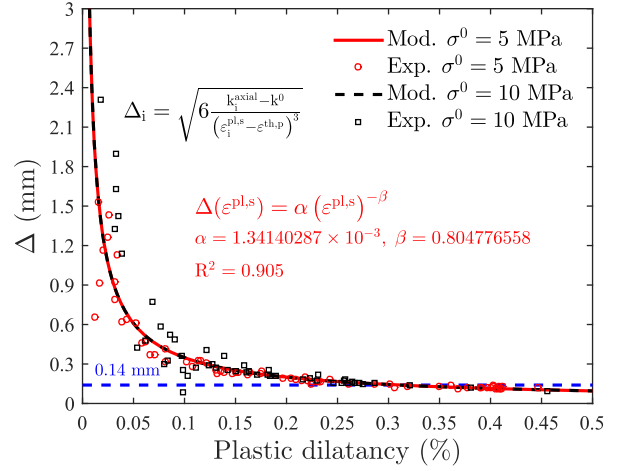


**Fig. 19.** Evolution of the equivalent crack spacing for mortar with respect to plastic dilatancy.

decreases significantly when plastic dilatancy was lower than 0.3%. When dilatancy was greater than 0.3%, an asymptotic value of 0.14 mm was reached.

The stage where  $\Delta$  decreases can be attributed to the increasing number of cracks,  $n$ , for a small loading rate. After this stage, the number of cracks does not increase any more. In this situation, the increase of permeability can be attributed to the increase of crack openings only (considering  $\Delta$  constant).

Fig. 17 represents the evolution of the permeability variations with respect to the total expansion considering the asymptotic value of 0.14 mm for  $\Delta$ . This led to a permeability being slightly underestimated when radial strain was lower 0.3%. However, it could be possible to improve these results by considering  $\Delta$  as a function of dilatancy as shown in Fig. 20.

We recall that the effects of crack tortuosity were not considered but could be roughly taken into account by introducing a reduction factor,  $\xi$ , when computing the crack permeability (20). For instance, for ordinary mortar (OM),  $\xi$ , was found to be equal 0.229 [5]. This assumption would increase the asymptotic crack spacing to ( $\Delta = 0.3$  mm), which might be more realistic because it is closer to the size of grains of sand. For instance, the size of fine sand and coarse sand used in [9] were [0.16–2] and [0.8–3.15] mm, respectively.

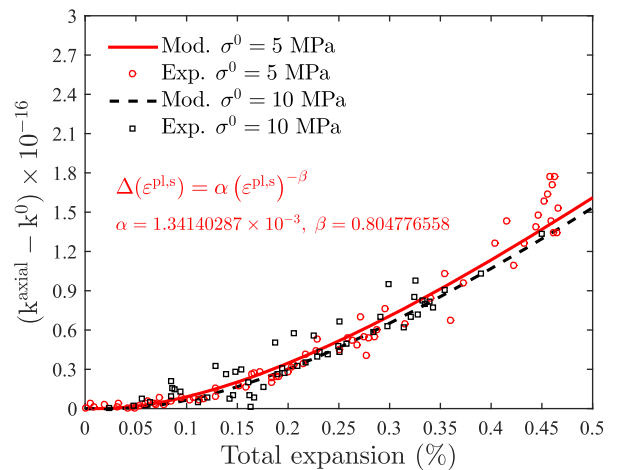


**Fig. 20.** Evolution of the absolute permeability variation for mortar with respect to the total expansion:  $\Delta$  was assumed function of dilatancy.

**Table 4**  
Mechanical parameters for simulation of triaxial test on granite.

Mechanical parameter	Symbol	Value	Unit
Initial Young's modulus	$E^0$	46000	MPa
Initial Poisson's ratio	$\nu^0$	0.15	
Compression peak strength	$R^c$	230.4	MPa
Strain at $R^c$	$\varepsilon^{\text{peak},c}$	$9.10^{-3}$	
Characteristic strain	$\varepsilon^{k,s}$	$3.5 \times 10^{-3}$	
Dilatancy coefficient	$\beta$	0.45	
Drucker–Prager coefficient	$\delta$	1.15	

### 3.2.2. Granite triaxial test simulation

This section reports a triaxial test performed on granite. In a manner comparable to the one described in [9], axial gas permeability measurements were performed on Beishan granite (a rock located in China and extracted at 500 m depth, intended for a nuclear waste repository). Cylindrical specimens 50 mm in diameter and 100 mm height were subjected to triaxial load [32].

The granite mechanical parameters considered for this study are noted in Table 4.

When the confining pressure was 8 MPa, the experimental deviatoric peak strength was 277.6 MPa, but, when the confining pressure was 10 MPa, the experimental deviatoric peak strength was 289.4 MPa [32]. According to the Drucker–Prager criterion, this led to  $R^c = 230.4$  MPa and allowed to the friction angle to be deduced:  $\phi = 48.32$  deg, and so  $\delta = 1.15$ . As, for this simulation,  $\varepsilon^{\text{peak},c}$  was chosen to fit the axial experimental results (positive parabolic hardening behaviour) and  $\beta$  was chosen to make dilatancy compatible with radial measurements (expansion), the same values as before were found for concrete and mortar:  $\beta = 0.45$ . Since  $\beta$  was found to be equal for concrete, mortar and granite, the value of  $\varepsilon^{k,s}$ , controlling the evolution of damage with regard to dilatancy was kept unchanged.

Fig. 21 presents the evolutions of deviatoric stress with respect to axial and radial strains obtained under different confining pressures,  $\sigma^0$ , (8 and 10 MPa). The mechanical model was then able to give moderately good agreement with experimental data [32]. The results were not as relevant as those obtained for concrete and mortar in Figs. 9 and 16, as the granite samples were taken at 500 m depth, where the stress field was close to 9, 13 and 13.5 MPa, in the minor horizontal,  $\sigma_h$ , major horizontal,  $\sigma_H$ , and vertical,  $\sigma_v$ , directions, respectively [32]. Consequently, the decon-

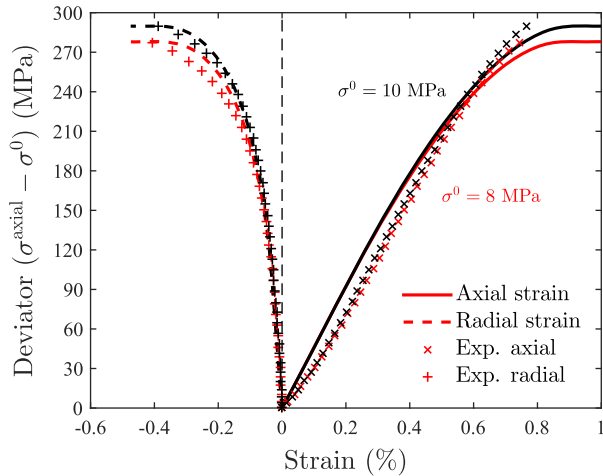


**Fig. 21.** Evolutions of granite deviatoric stress with respect to axial and radial strains for different confining pressures (8 and 10 MPa). Comparison with measurements [9].

**Table 5**  
Hydraulic parameters for simulation of triaxial test on granite.

Hydraulic parameter	Symbol	Value	Unit
Intrinsic permeability ( $\sigma^0 = 8$ MPa)	$k^0$	$4.6 \times 10^{-19}$	$\text{m}^2$
Intrinsic permeability ( $\sigma^0 = 10$ MPa)	$k^0$	$7.1 \times 10^{-20}$	$\text{m}^2$
Strain percolation threshold	$\varepsilon^{\text{th},p}$	$0.13\varepsilon^{\text{peak},c}$	
Equivalent crack spacing	$\Delta$	0.145	mm

finement process during extraction of specimens may have led to increased initial microcracking and thus to more pronounced stiffness restitution in the axial stress–strain curve, as shown in Fig. 21, corresponding to phase 1 described previously in Section 2.2. On the other hand, the radial strains predicted in Fig. 21, which were not affected by reclosure of microcracks, provided better agreement with measurements. In this case, radial strains were of greater importance because permeability measurements were made in the axial direction.

Table 5 introduces the hydraulic parameters considered for this study. This table indicates that the initial intrinsic permeabilities were not the same for both specimens tested in [32]. For this reason, the predicted axial permeabilities are compared to measurements in terms of absolute variation ( $k^{\text{axial}} - k^0$ ) in Fig. 22, as adopted for the mortar triaxial test, to extract the contribution of cracking independently of initial permeability.

Fig. 22 presents the experimental evolutions of the absolute permeability variations as found in [32], with respect to deviatoric stress. This figure indicates:

1. An increasing percolation threshold (with respect to deviatoric stress) for permeability (when  $\sigma^0$  increases). In a previous study on granite using an empirical damage permeability relationship, this phenomenon was taken into account by increasing the threshold damage parameter when  $\sigma^0$  increased, in order to delay the initiation of permeability variation [14]. The proposed model takes this phenomenon into account implicitly, through the Drucker–Prager criterion (3), which delays the initiation of plastic dilatancy when  $\sigma^0$  increases.
2. The decreasing permeability with respect to confinement also observed in experimental results [14,32] (for the same deviatoric stress) is again taken into account through the Drucker–Prager criterion.

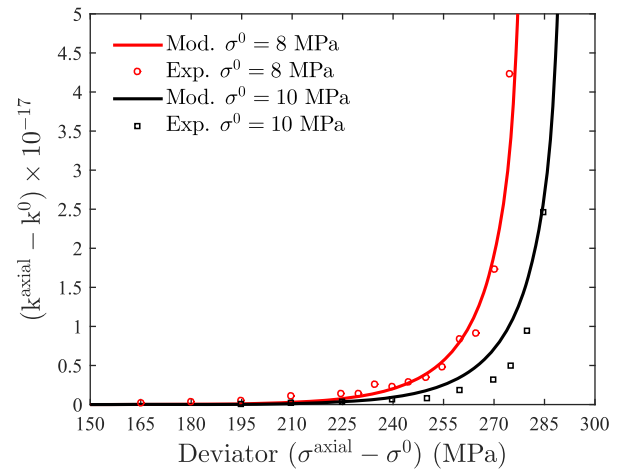


**Fig. 22.** Evolutions of granite absolute axial permeability ( $k^{\text{axial}} - k^0$ ) with respect to deviatoric stress for different confining pressures (8 and 10 MPa). Comparison with measurements [9].

**Table 6**  
Summary of the main parameters affecting mechanical and hydraulic responses

	$R^c$ (MPa)	$\delta$	$\beta$	Size of inclusions (mm)	$\Delta$ (mm)
Concrete	28.0	0.72	0.45	[4–12.5]	2.200
Mortar	84.4	1.16	0.45	[0.16–3.15]	0.140
Granite	230.4	1.15	0.45	[0.5–2.0]	0.145

It is worth noting that confinement affected permeability variations for granite because the results were represented in function of the deviatoric stress in Fig. 22. If the results were plotted in function of the expansion as in the previous study for mortar, the differences would disappear.

In order to fit the experimental permeability results in Fig. 22, an equivalent crack spacing ( $\Delta = 0.145$  mm) was found. As indicated in [32], granite is mainly made of 52% plagioclase (Pl), 17% quartz (Qtz), 15% K-feldspar (Kfs), 12% biotite (Bt), 3% albite (Ab) and 1% myrmekite (My) [14], where the size of minerals commonly ranges between 0.5 and 2 mm [32].

As mortar and granite have almost the same mineralogical heterogeneity, their permeability variations were found to be reasonably estimated considering a crack spacing of 0.140 mm and 0.145 mm, respectively.

Finally, the assumption that crack spacing increases with the size of “inclusions” was justified, as evidenced in Table 6.

#### 4. Conclusions

This work has been devoted to the damage and permeability interactions induced by plasticity in the case of damage leading to diffuse cracking.

In a first step, the literature review highlighted the necessity to consider plasticity, especially, dilatancy when modelling permeability variations under compression or deviatoric loading.

The proposed development was then embedded in an elastoplastic damage model allowing irreversible strains and dilatancy to be computed thanks to a non-associated Drucker–Prager criterion.

In a uniaxial compression test simulation, the permeability model was able to predict realistic results, as observed in the literature, especially for the anisotropy ratio of axial and radial permeabilities. More particularly, the axial permeability was found to be higher than the radial ones, as a consequence of expansion (dilatancy) leading to a diffuse crack pattern preferentially oriented parallel to the loading direction.

In triaxial test simulations, the permeability model was able to predict realistic results for both mortar and granite materials.

For mortar, the absolute permeability variations were found to be almost independent of the confining pressure,  $\sigma^0$ , when these variations were plotted versus radial strain. This justified the computing of permeability in function of dilatancy, according to Poiseuille's law in system (17).

For granite, the decreasing permeability with respect to confining pressure,  $\sigma^0$ , was found as observed experimentally.

Finally, a correlation between the size of “inclusions” in geomaterials and crack spacing can be proposed as an explanation for  $\Delta$ . It led to a decreasing crack spacing when the size of the “inclusions” decreases and this was in agreement with the size of concrete aggregates, grains of sand and granite minerals. However further investigation are required (experimental plan and/or homogenization method) in order find an appropriate relation that may predict an estimation of crack spacing according to the average distribution of “inclusions”.

#### Acknowledgements

The authors gratefully acknowledge the financial support of the French Ministry of Education and University of Nantes.

#### References

- [1] K. Wang, D. Jansen, S. Shah, A. Karr, Permeability study of cracked concrete, *Cem. Concr. Res.* 27 (3) (1997) 381–393.
- [2] C. Aldea, S. Shah, A. Karr, Permeability of cracked concrete, *Mater. Struct.* 32 (1999) 370–376.
- [3] C. Aldea, M. Ghandehari, S. Shah, A. Karr, Estimation of water flow through cracked concrete under load, *ACI Mater. J.* 97 (5) (2000) 567–575.
- [4] V. Picandet, A. Khelidj, H. Bellegou, Crack effects on gas and water permeability of concretes, *Cem. Concr. Res.* 39 (6) (2009) 537–547.
- [5] A. Akhavan, S. Shafaatian, F. Rajabipour, Quantifying the effects of crack width, tortuosity, and roughness on water permeability of cracked mortars, *Cem. Concr. Res.* 42 (2) (2012) 313–320.
- [6] G. Rastello, C. Boulay, S. Dal Pont, J.L. Tailhana, P. Rossi, Real-time water permeability evolution of a localized crack in concrete under loading, *Cem. Concr. Res.* 56 (2014) 20–28.
- [7] T. Sugiyama, T.W. Bremner, T.A. Holm, Effect of stress on gas permeability in concrete, *ACI Mater. J.* 93 (1996) 443–450.
- [8] N. Hearn, G. Lok, Measurement of permeability under uniaxial compression, *ACI Mater. J.* 95 (1998) 691–694.
- [9] H. Meziani, F. Skoczylas, An experimental study of the mechanical behaviour of a mortar and of its permeability under deviatoric loading, *Mater. Struct.* 32 (1999) 403–409.
- [10] V. Picandet, A. Khelidj, G. Bastian, Effect of axial compressive damage on gas permeability of ordinary and high-performance concrete, *Cem. Concr. Res.* 31 (2001) 1525–1532.
- [11] O. Schulze, T. Popp, H. Kern, Development of damage and permeability in deforming rock salt, *Eng. Geol.* 61 (2001) 163–180.
- [12] M. Choinska, *Effet de la température, du chargement mécanique et de leurs interactions sur la perméabilité du béton de structure* (Ph.D. thesis), École centrale de Nantes, 2006.
- [13] M. Choinska, A. Khelidj, G. Chatzigeorgiou, G. Pijaudier-Cabot, Effects and interactions of temperature and stress-level related damage on permeability of concrete, *Cem. Concr. Res.* 37 (2007) 79–88.
- [14] L. Chen, J.F. Liu, C.P. Wang, J. Liu, R. Su, H. Wang, Characterization of damage evolution in granite under compressive stress condition and its effect on permeability, *Int. J. Rock Mech. Min. Sci.* 71 (2014) 340–349.
- [15] H. Wang, W. Xu, J. Shao, F. Skoczylas, The gas permeability properties of low-permeability rock in the process of triaxial compression test, *Mater. Lett.* 116 (2014) 386–388.
- [16] L. Jason, G. Pijaudier-Cabot, S. Ghavarian, A. Huerta, Hydraulic behaviour of a representative structural volume for containment buildings, *Nucl. Eng. Des.* 237 (2007) 1259–1274.
- [17] E. Bourdarot, *Application of a porodamage model to analysis of concrete dams*, Tech. rep. EDF/CNEH, 1991.
- [18] B. Bary, *Étude du couplage hydraulique-mécanique dans le béton endommagé* (Ph.D. thesis), ENS Cachan, 1996.
- [19] D. Gawin, F. Pesavento, B.A. Schrefler, Simulation of damage-permeability coupling in hygro-thermo-mechanical analysis of concrete at high temperature, *Commun. Numer. Methods Eng.* 18 (2002) 113–119.
- [20] B. Bary, J.-P. Bournazel, E. Bourdarot, Poro-damage approach applied to hydro-fracture analysis of concrete, *J. Eng. Mech.* 126 (2000) 937–943.
- [21] B. Gérard, D. Breyse, A. Ammouche, O. Houdusse, O. Didry, Cracking and permeability of concrete under tension, *Mater. Struct.* 29 (3) (1996) 141–151.
- [22] A. Sellier, G. Casaux-Ginestet, L. Buffo-Lacarrière, X. Bourbon, Orthotropic damage coupled with localized crack reclosure processing: Part I: constitutive laws, *Eng. Fract. Mech.* 97 (2013) 148–167.
- [23] CAST3M 2015 Finite Element Program, <http://www-cast3m.cea.fr/>.
- [24] S. Dal Pont, A. Ehrlacher, Numerical and experimental analysis of chemical dehydration, heat and mass transfer in a concrete hollow cylinder submitted to high temperatures, *Int. J. Heat Mass Transfer* 47 (1) (2004) 135–147.
- [25] G. Pijaudier-Cabot, F. Dufour, M. Choinska, Permeability due to the increase of damage in concrete: from diffuse to localized damage distributions, *J. Eng. Mech.* 135 (2009) 1022–1028.
- [26] M. Oda, T. Takemura, T. Aoki, Damage growth and permeability change in triaxial compression tests of Inada granite, *Mech. Mater.* 34 (2002) 313–331.
- [27] K. Maleki, A. Pouya, Numerical simulation of damage-permeability relationship in brittle geomaterials, *Comput. Geotech.* 37 (2010) 619–628.
- [28] W. Chen, C. La Borderie, O. Maurel, G. Pijaudier-Cabot, F. Rey-Bethbeder, Simulation of damage-permeability coupling for mortar under dynamic loads, *Int. J. Numer. Anal. Methods Geomech.* 38 (2014) 457–474.
- [29] N. Burlion, F. Bourgeois, J.-F. Shao, Effects of desiccation on mechanical behaviour of concrete, *Cem. Concr. Compos.* 27 (2005) 367–379.
- [30] E. Öztekin, S. Pul, M. Hüsem, Experimental determination of Drucker–Prager yield criterion parameters for normal and high strength concretes under triaxial compression, *Constr. Build. Mater.* 112 (2016) 725–732.
- [31] J.J. Zhou, J.F. Shao, W.Y. Xu, Coupled modeling of damage growth and permeability variation in brittle rocks, *Mech. Res. Commun.* 33 (2006) 450–459.
- [32] Y. Chen, S. Hu, K. Wei, R. Hu, C. Zhou, L. Jing, Experimental characterization and micromechanical modeling of damage-induced permeability variation in Beishan granite, *Int. J. Rock Mech. Min. Sci.* 71 (2014) 64–76.
- [33] A. Sellier, A. Millard, Weakest link and localisation  $WL^2$ : a method to conciliate probabilistic and energetic scale effects in numerical models, *Eur. J. Environ. Civ. Eng.* 18 (2014) 1177–1191.